Specific targeting of brain tumors with an optical/MR imaging nanoprobe across the blood brain barrier

Omid Veiseh[1], **Conroy Sun**[1], **Chen Fang**[1], **Narayan Bhattarai**[1], **Jonathan Gunn**[1], **Forrest Kievit**[3], **Kim Du**[3], **Barbara Pullar**[5], **Donghoon Lee**[2], **Richard G. Ellenbogen**[4,6], **Jim Olson**[5,6], and **Miqin Zhang**[1,2,4,*]

[1]Department of Materials Science & Engineering, University of Washington, Seattle, Washington 98195, USA

[2]Department of Radiology, University of Washington, Seattle, Washington 98195, USA

[3]Department of Bioengineering, University of Washington, Seattle, Washington 98195, USA

[4]Department of Neurological Surgery, University of Washington, Seattle, Washington 98195, USA

[5]Clinical Research Division, Fred Hutchinson Cancer Research Center, Seattle, Washington 98109, USA

[6]Seattle Children's Hospital & Regional Medical Center, Seattle, Washington 98105, USA

Abstract

Nanoparticle-based platforms have drawn considerable attention for their potential impact on oncology and other biomedical fields. However, their *in vivo* application is challenged by insufficient accumulation and retention within tumors due to limited specificity to the target, and an inability to traverse biological barriers. Here we present a nanoprobe that demonstrates an ability to cross the blood-brain barrier and specifically target brain tumors in a genetically engineered mouse model, as established through *in vivo* MR and biophotonic imaging, and histological and biodistribution analyses. The nanoprobe is comprised of an iron oxide nanoparticle coated with biocompatible PEG-grafted chitosan, to which a tumor targeting agent, chlorotoxin and a near infrared fluorophore are conjugated. The nanoprobe demonstrates an innocuous toxicity profile and sustained retention in tumors. With the versatile affinity of the targeting ligand and the flexible conjugation chemistry for alternative diagnostic and therapeutic agents, this nanoparticle platform can be potentially used for diagnosis and treatment of a variety of tumor types.

Keywords

nanoparticle; brain tumor; MRI; targeting; blood brain barrier

Introduction

Nanoparticle based diagnostic and therapeutic platforms have been investigated extensively due to their potential impact on clinical oncology for early detection, treatment, and staging of tumors (1,2). Particularly, the use of magnetofluorescent nanoprobes, combined with both high spatial resolution MR and quantitative biophotonic fluorescence imaging, could allow for more

versatile use of these nanoparticles. However, the implementation of this approach is complicated by the inability of current generation contrast agents to circumvent biological barriers, such as the blood brain barrier (BBB) and vascular endothelium, as well as the non-specific uptake by surrounding tissues and macrophages upon intravenous injection (3,4).

Serving as the major interface between blood and brain, the BBB is responsible for transporting essential nutrients and metabolites to the brain while protecting and regulating its internal environment. As such, the BBB represents one of the most exclusive biological barriers encountered in the treatment of neurological diseases, limiting the delivery of a vast majority of potential diagnostic agents and therapeutics (5,6). Although the specific mechanisms for BBB passage have yet to be elucidated, strategies such as the integration of lipophilic substances have been shown to facilitate passive diffusion of macromolecules into the brain parenchyma (7,8). Alternatively, attachment of ligands such as apolipoproteins (9,10), transferrin antibiodies (11,12), TAT peptide (13), or alpha methyl tryptophan (14), and of positively charged moieties has been reported to promote receptor-mediated and adsorptive-mediated transcytosis for macromolecules to cross the BBB (7,15,16). Recent studies in polymeric and liposome nanoparticles indicated that BBB passage by nanoparticulates was dictated by hydrodynamic size, charge, and surface chemistry of the particles (10,17–23). For example, a recent study evaluated the influence of the nanoparticle size on BBB permeability and showed that gadolinium chelated dendrimer nanoparticles with core sizes smaller than 12 nm were able to permeate the blood brain tumor barrier while those with large sizes were hindered (20). Cationic albumin nanoparticles have been investigated in many studies and were shown effective in permeating the BBB due to their cationic charge (21,22). Another recent study demonstrated that the hydrophilicity of polymeric nanoparticles could influence BBB permeability (23). Although these advances are encouraging, they were limited to passive delivery of nanoparticles (i.e. inability to specifically target tumor), and provided limited information about the influence of nanoparticles on the BBB integrity and on safe profile of these constructs. None, to our knowledge, has been demonstrated to deliver imaging contrast agents specifically to brain tumors. Given the shortcomings of conventional Gd-DTPA based MR imaging, including non-specific tissue contrast and quick clearance (24), the development of a nanoparticle-based imaging agent to overcome these challenges would fulfill a significant clinical need.

Here we report the development of a targeting nanoprobe that is capable of selectively accumulating in brain tumors across the BBB. We integrated a number of design elements in the development scheme of this nanoprobe that would facilitate the BBB crossing and tumor-specific targeting, including synthesizing core nanoparticles with minimal size, coating nanoparticles with a thin but dense polymer layer, integrating ample chemical functionality, employing a small, versatile tumor-specific ligand, and use of biocompatible materials. The nanoprobe (NPCP-CTX-Cy5.5) is comprised of an iron oxide nanoparticle (NP) coated with a PEGylated-chitosan branched copolymer (CP), to which a targeting ligand, chlorotoxin (CTX) and a near-infrared fluorophore, Cy.5.5 were conjugated (Fig. 1). In this design, chitosan is utilized as a linker and stabilizer. The amino and hydroxyl groups of chitosan's glucosamine backbone serve to anchor the polymer to the iron oxide surface through electrostatic interaction and physical adsorption alleviating the need for crosslinking agents while providing sites for subsequent conjugation of ligands without the need for further chemical modification. The bound chitosan also acts as a sterically stabilizing corona, preventing particle aggregation under physiological conditions. *In vivo*, aggregated or opsonized nanoparticles are readily recognized and rapidly cleared from the bloodstream by the reticuloendothelial system (RES) prior to reaching target tissues (25). PEG is integrated into the polymer coating to reduce protein adsorption, limit immune recognition, and thereby increase the nanoprobe serum half-life *in vivo*. In addition to its magnetic property for MRI detection, the nanoparticle coated with the PEGylated-chitosan branched copolymer (NPCP) received selective targeting and optical

functionality via covalently linked CTX and Cy5.5, respectively. CTX, a 36 amino acid peptide, was selected as a tumor targeting ligand due to its strong affinity for tumors of the neuroectodermal origin (26,27). We previously showed that CTX specifically binds to glioma, medulloblastoma, prostate cancer, sarcoma, and intestinal cancer (28). Integration of Cy5.5 into nanoparticle coating, combined with the presence of the intrinsic superparamagnetic core, makes the nanoprobe a dual contrast agent, detectable by both MR and biophotonic imaging, which expands the scope of its applicability. The NPCP provides flexible functional groups for conjugation of any ligands bearing either amine groups or sulfhydryl groups, including CTX and Cy5.5 demonstrated in this study.

In addition to the favorable physiochemical properties, these constituents are also selected to facilitate the BBB crossing by the nanoprobe. Amphiphilic PEG with high lipid solubility may increase the endothelial permeability of the nanoprobe and thus facilitate its BBB passage. PEG has been shown to facilitate the BBB permeability of several conjugates (15,29–31). Positively charged cationic chitosan may interact with the negatively charged brain endothelium via electrostatic interactions to trigger adsorptive-mediated transport across the BBB. Also, the small hydrodynamic size of the nanoprobe is essential for the BBB passage (32,33). CTX has also been observed to permeate an intact BBB in both animal models and humans with brain tumors (28,34). We evaluated the capability of this nanoprobe to transverse the BBB, its tumor-specific targeting efficiency and MRI and optical detectability in a transgenic mouse model, ND2:SmoA1, that closely resembles human medulloblastoma, the most common malignant childhood brain tumor (35). The medulloblastomas arise spontaneously in the cerebellum (36) and maintain an intact BBB (28).

Materials and Methods

Nanoprobe synthesis

PEG was grafted onto chitosan by alkylation of depolymerized chitosan followed by Schiff base formation (37). Depolymerized chitosan was obtained by oxidative degradation of high molecular weight chitosan (Mw = 190 kDa, Sigma, St. Louis, MO) with sodium nitrite (NaNO$_2$). The chitosan depolymerization was carried out by reacting 100mM aqueous NaNO$_2$ solution with a 2 wt% chitosan solution (pH = 4.5, dilute acetic acid) for 24 hrs at room temperature. Methoxy PEG (Mn = 2000 g/mole, Sigma) was first oxidized into PEG-aldehyde and then reacted with primary amines of depolymerized chitosan in the presence of sodium cyanoborohydride. Chemical structure and purity of the polymer were confirmed by HPLC and ^{1}H-NMR.

The nanoparticles were synthesized in the presence of chitosan grafted PEG (the chitosan-g-PEG) via co-precipitation of ferrous and ferric chlorides with ammonium hydroxide. Specifically, NPCP were synthesized by first dissolving 3.0 g of PEGylated chitosan in 50 ml deionized H$_2$O followed by addition of an iron chloride solution (4.6 g FeCl$_2$·H$_2$O and 9.1 g FeCl$_3$ dissolved in 50 ml of deoxygenated deionized H$_2$O). This mixture was then heated to 40°C under mechanical stirring and nitrogen bubbling. One hundred millilitres of 7% NH$_4$OH was then added to the polymer and iron chloride mixture at a rate of 100 ml per hr. The resulting black precipitate was dialyzed for 2–3 days in H$_2$O to remove unreacted reagents.

CTX (Alamone Labs, Jerusalem, Israel) and Cy5.5 (GE Healthcare, Piscataway, NJ) were conjugated to the NPCP through the chemical scheme outlined in Figure 1a. Specifically, 1.75 mg of monoreactive Cy5.5 NHS ester was dissolved in 100 µl of anhydrous dimethyl formamide (DMF, Sigma, St. Louis, MO) and the solution was then added to 2 ml NPCP (2.5 mg of Fe/ml, suspended in 0.1M sodium bicarbonate pH 8.5). The suspension was allowed to react for 2 hrs prior to the addition of 100 µl of succinimidyl iodoacetate (SIA; Molecular Biosciences, Boulder, CO; 50 mg/ml, dissolved in anhydrous DMSO). The resulting solution

was allowed to react for an additional 2 hrs. Excess Cy5.5 and SIA were removed from the suspension through gel chromatography using Sephacryl S-200 column (GE Healthcare) equilibrated with 20mM sodium citrate, 0.15M NaCl buffer at pH 8.0. CTX was functionalized with sulfhydryl groups through reaction with *N*-succinimidyl-S-acetylthioacetate (SATA; Molecular Bioscience). To perform this reaction, 40 µl of SATA (1 mg/ml, dissolved in anhydrous DMSO) was added to a 1 ml solution of CTX (1 mg/ml, dissolved in 50 mM bicarbonate buffer, pH 8.5). After reaction for 1 hr at room temperature excess SATA was removed by dialysis against PBS buffer (pH 7.4). Upon purification, SATA was deprotected by reacting 100 µl of a 25 mM hydroxylamine with 10 mM EDTA solution for 1 hr at room temperature. The resulting sulfhydryl modified peptide was then added to the Cy5.5 and SIA modified NPCP solution, and the mixture was allowed to react for 1 hr at room temperature. Unreacted CTX was removed from the suspension through gel filtration chromatography using Sephacryl S-200 column equilibrated with 20mM sodium citrate, 0.15M NaCl buffer at pH 8.0.

Animal model

All mouse studies were conducted with procedures approved by the Institutional Animal Care and Use Committee at the University of Washington and Fred Hutchinson Cancer Research Center (FHCRC). Transgenic ND2:SmoA1 mice were generated on a C57BL/6 background (Charles River Laboratories Inc., Wilmington, MA) as described previously (36). Non-genetically altered C57BL/6 mice were used as wild-type controls. Symptomatic and wild-type mice were injected with nanoprobes at 10 mg/kg (n = 3) for *in vivo* MR and optical studies.

In vivo MR imaging

Multi-echo multi-slice imaging was performed on a 4.7 T magnet. Spin-spin relaxation time T2 maps were generated by multi-echo images with TE ranging from 14 to 68 ms. Details on imaging processing are provided in Supplementary Methods and Discussion. Spin-lattice relaxation time (T1) weighted MR imaging was performed for N2:SmoA1 mice before and after the injection of Gd-DTPA to confirm that the BBB is intact in the tumor-bearing mouse model. T1-weighted images were consecutively acquired five times prior to Gd-DTPA injection to obtain baseline signal intensities. Serial acquisitions of T1-weighted images were conducted for 60 min post intravenous injection of Gd-DTPA (0.1 mM/kg gadopentetate dimeglumine; 5× diluted Magnevist; injection volume = 100 µl; Berlex Laboratories, Wayne, NJ). The imaging parameters for T1-weighted images are as follows: TR/TE = 500/14.7 ms, number of averaging = 2, matrix = 256 × 128, slice thickness = 1.5 mm and acquisition time = 2 min. A mouse head coil and a head holder were utilized to image the N2:SmoA1 mice. A slice covering a tumor developed region was selected from 8 consecutive slices for each acquisition. Signal intensities were measured on two different regions of interest: one in the cerebellum region and the other outside the brain. Identical experiments were performed on the same mice 48 hrs post injection of NPCP-CTX nanoprobe.

In vivo optical imaging

Biophotonic fluorescence images were acquired on a Xenogen IVIS −100 system (Cliper Life Sciences, Hopkinton, MA). Mice were anesthetized with 2.5% isoflurane (VEDCO. Inc, MO) before they were placed in the imaging chamber and imaged before and at various time points after injection of the nanoprobe. Relevant organs, tissues, and tumors were dissected from some of the animals and imaged immediately to determine biodistribution. Fluorescence emission was normalized to photons per second per centimeter squared per steradian (p/s/cm^2/sr).

Histology and microscopy

The whole brains of mice were dissected immediately after the animals were sacrificed and fixed in freshly prepared 10% buffered formalin. Samples were then embedded in paraffin blocks. Half of the each brain was sliced along the sagittal plane into 10 µm sections and the remaining half was sliced along coronal plane, followed by staining with H&E and Prussian blue/Nuclear Fast Red per standard clinical laboratory protocol. Microscopic images of tissue were acquired using an E600 upright microscope (Nikon, Melville, NY) equipped with a CCD color camera.

Statistical analysis

The data were expressed as mean ± standard deviation of the mean. A paired t-test was used to determine significance of nanoprobe accumulation as measured by MR imaging. Statistical significance in biodistribution and toxicity effects were determined using one-way analysis of variance (ANOVA) followed by a Student's t-test for multiple comparison tests. We considered a P-value < 0.05 as statistically significant.

Results and Discussion

Synthesis and characterization of nanoprobes

PEGylated-chitosan branched copolymer (CP) was prepared by a process of chitosan alkylation followed by Schiff base formation, as reported in our previous work (37) (Fig. 1a, Reaction i). CTX was first functionalized with sulfhydryl groups through reaction with N-succinimidyl-S-acetylthioacetate (SATA) (Fig. 1a, Rection ii). Iron oxide nanoparticles (NP) were then synthesized through a co-precipitation process and simultaneously coated *in situ* with the copolymer CP (Fig. 1a, Reaction iii). The functionalized CTX and Cy5.5 were then conjugated to the NPCP via iodoacetate and amide linkages (Fig. 1a, Reaction iii), respectively, yielding an average of 16.2 CTX peptides and 1.5 fluorophores per NPCP (Fig. 1b), as determined by BCA protein quantification and fluorescence quantification, respectively (38). The mean hydrodynamic size and zeta potential of the resulting nanoparticle coated with CP (NPCP) was found to be 33 nm and 4.2 mV, respectively, by dynamic light scattering (DLS) (Fig. 1b and Supplementary Fig. 1). Transmission electron microscopy (TEM) of the NPCP (Supplemental Fig. 1, inset) showed the iron oxide cores with a mean diameter of 7 nm. It should be noted that this diameter differs from the hydrodynamic size in that the latter includes the contribution of the polymer coating and hydration of the PEG chains in aqueous solution. Powder X-ray diffraction (XRD) of the NPCP (Fig. 1c) is consistent with that of crystalline magnetite (Fe_3O_4; JCPDS card No. 19–0629), while immobilization of the copolymer on the iron oxide surface was confirmed by Fourier transformed infrared (FTIR) spectroscopy (Fig. 1d and Supplementary Methods and Discussion). In addition, the number of reactive amino functional groups on each NPCP was quantified by N-succinimidyl 3-(2-pyridyldithio)-propionate (SPDP) assay and determined to be 30.5 primary amines per NP. Nanoparticles coated with CP were found to be stable (i.e., no agglomeration or loss of functionality) in solutions of physiological pH for months compared to those coated with chitosan alone which demonstrated a short shelf-life of a few hours under identical conditions.

To verify targeting specificity of CTX-conjugated NPCP (NPCP-CTX) for brain tumor cells, *in vitro* cell uptake experiments were performed. When incubated with 9L rat gliosarcoma cells, NPCP-CTX showed a 6.1 ± 1.1 (mean ± s.d. $P < 0.0001$)-fold increase in uptake compared with the non-targeting control nanoprobe (NPCP), and an 11 ± 0.8 (mean ± s.d. $P < 0.0001$)-fold increase compared with dextran-coated nanoparticles (NP-Dextran) (Supplementary Fig. 2). Furthermore, the effectiveness of the PEG conjugated on nanoprobe on suppressing macrophage uptake of the nanoprobe was also evaluated *in vitro*. Uptake of NPCP by RAW

264.7 macrophages was found to be 12.4 ± 0.7 (mean $\pm$ s.d. $P < 0.0001$)-fold lower than that of nanoparticles coated with chitosan alone (NPC) (Supplementary Fig. 3).

Evaluation of MR imaging contrast enhancement and in vivo MR imaging

The magnetic properties of the nanoprobe were evaluated by MR imaging utilizing the clinically approved, dextran-coated iron oxide nanoparticle, Feridex I.V.®, as a reference. MR images of agarose samples containing NPCP of varying concentrations (Supplementary Fig. 4a) were acquired over a range of echo times (TE) to generate a R2 (1/T2) map (Supplementary Fig. 4b). A linear correlation of R2 with particle concentration was observed for both contrast agents (Supplementary Fig. 4c). The r2 relaxivities (slope of R2 vs. particle concentration) for NPCP and Feridex I.V.® were $472.3 \text{ s}^{-1}\text{mM}^{-1}$ and $243.3 \text{ s}^{-1}\text{mM}^{-1}$, respectively. The higher relaxivity exhibited by NPCP in comparison to the commercial agent qualifies NPCP as a valid MRI contrast agent.

MR imaging was used to demonstrate the specific targeting capability of NPCP-CTX nanoprobe to tumors *in vivo* and validate the nanoprobe as an MRI contrast agent. The MR imaging was performed on symptomatic ND2:SmoA1 (Fig. 2a) and wild-type mice (as an animal control, Fig. 2b) receiving either targeting NPCP-CTX or non-targeting NPCP (as a particle control), each administered via tail vein injection. Coronal MR images of the frontal lobe of the cerebral hemisphere (healthy tissue) and cerebellum (tumor-containing tissue) were acquired over a range of TEs (14 to 68 ms) prior to nanoprobe injection and at 48 hrs post-injection. Utilizing these series of images, R2 maps were generated and overlaid on proton density images to analyze nanoprobe accumulation. 48 hrs after injection of targeting NPCP-CTX, the significant increase in R2 (red coloration) at the periphery of the cerebellum in ND2:SmoA1 mice, as compared with the image taken prior to injection, indicated specific nanoprobe accumulation (Fig. 2a, first column of left panel), while images of the frontal lobe region of these mice did not show discernible R2 shifts between pre- and post-injection of NPCP-CTX (Fig. 2a, second column of left panel), indicating minimal or no accumulation of the nanoprobes in healthy brain tissues. This result confirms that the targeting nanoprobe preferentially accumulate in neoplastic tissues. The areas highlighted by NPCP-CTX in the cerebellum coincide well with the tumor regions identified in histological sections of the same tissue slices stained with haematoxylin and eosin (H&E; Supplementary Fig. 5).

Quantitative evaluation of NPCP-CTX accumulation further indicated a contrast enhancement of $37.6 \pm 2.4\%$ (mean $\pm$ s.d.), in term of R2 increase, in the cerebellum, while minimal contrast variations in healthy tissue of the frontal lobe were found before and after nanoprobe injection ($4.3 \pm 1.6\%$, $P < 0.0001$) (Fig. 2c). No apparent contrast enhancement was observed in either the cerebellum or frontal lobe of ND2:SmoA1 mice treated with non-targeting NPCP (Fig. 2a, right panel). Quantitative evaluation also found minimal or no contrast change ($P > 0.05$) in both cerebellum ($0.7 \pm 0.9\%$) and frontal lobe ($1.2 \pm 2.5\%$) of ND2:SmoA1 mice receiving NPCP (Fig. 2c). This result indicates that the NPCP has no specific targeting capability due to lack of targeting ligand CTX.

Specific targeting of the NPCP-CTX nanoprobe to tumors was further counter-illustrated with wild-type mice (bearing no tumors) injected with these nanoprobes, which showed no apparent NPCP-CTX accumulation in the brain (Fig. 2b, left panel). Non-targeting NPCP also showed no apparent accumulation in wild-type mice, as expected (Fig. 2b, right panel). Quantitative evaluation of both the targeting and control nanoprobes in wild-type mice further confirmed no significant change in R2 in either frontal lobe ($P > 0.05$) or cerebellum ($P > 0.05$) regions after nanoprobe injection (Fig. 2d).

In vivo optical imaging and histology

The ability of the NPCP-CTX nanoprobe to specifically target tumors and serve as an optical contrast agent was assessed by quantitative *in vivo* imaging experiments using NIRF imaging with Cy5.5 attached to NPCP-CTX (NPCP-Cy5.5-CTX). First, we determined the correlation between nanoprobe concentration and optical intensity of fluorescence emission, which revealed a linear relation (Supplementary Fig. 6). Then, specific tumor targeting and illumination in symptomatic ND2:SmoA1 mice by the targeting nanoprobe was assessed at 2 and 120 hrs (Fig. 3a and 3b, respectively) post-injection of either targeting NPCP-Cy5.5-CTX or its non-targeting variant, NPCP-Cy5.5 (as control). Preferential accumulation of the NPCP-Cy5.5-CTX in tumors was evident by the significant NIRF signal observed only in the brain tumor regions of the mice receiving NPCP-Cy5.5-CTX at both 2 and 120 hrs (the first mouse in Fig. 3a and 3b, respectively) post-injection. Quantitative analysis of NIRF signal intensity revealed that the accumulation of NPCP-Cy5.5-CTX nanoprobe in the brain tumor was complete by 50 hrs post-injection and that the signal intensity remained at a similar level throughout the remaining 70 hrs of the 120 hour analysis (Supplementary Fig. 7), indicating prolonged retention of NPCP-CTX-Cy5.5 in tumors. Conversely, significantly lower levels of NIRF signal were detected in the tumors of mice receiving non-targeting NPCP-Cy5.5 2 hrs post-injection (the second mouse in Fig. 3a) followed by no detectable signal after 50 hrs post injection (Supplementary Fig. 7 and the second mouse in Fig. 3b). The mice receiving no injection were also presented as references (the third mouse in Fig. 3a and 3b, and Supplementary Fig. 7). *Ex vivo* images of the brains of mice receiving NPCP-Cy5.5-CTX were acquired immediately after whole-body optical imaging of mice, which showed a NIRF signal outlining the medulloblastoma tumor regions (Fig. 3b, inset, the first mouse), demonstrating the ability of this probe to potentially serve as an aid in intra-operative tumor resection. Conversely, no significant levels of fluorescence were detected in the brains of mice receiving the NPCP-Cy5.5 (Fig. 3b, inset, the second mouse). These results correlate well with those obtained from MR imaging (Fig. 2), confirming the selective accumulation of targeting nanoprobes (but not non-targeting nanoprobes) in tumors.

To determine the accuracy of the regions highlighted as tumor tissue by the NPCP-Cy5.5-CTX nanoprobe, histological analysis (Fig. 4) was performed on the excised brains of the mice after the NIRF imaging. The dark purple region in the H&E stained cerebellum of the ND2:SmoA1 mice clearly outlines the tumor (Fig. 4a), which is absent in the comparable brain sections from the wild-type mouse (Fig. 4b). Higher magnification images of the H&E stained ND2:SmoA1 mouse brain sections show the difference in cell density and morphology between tumor and healthy tissues (Fig. 4c, first row). The selective accumulation of the NPCP-CTX-Cy5.5 nanoprobe within tumor tissue was evident by the positive iron staining of Prussian blue which is absent in the healthy tissue (Fig. 4c, second row). This result further indicates that the regions illuminated by the nanoprobe in the *in vivo* optical imaging were neoplastic in nature and nanoparticles accumulated in neoplastic tissue but not in healthy tissue. Brains excised from ND2:SmoA1 mice receiving NPCP-Cy5.5 showed no apparent nanoprobe accumulation in either tumor or normal brain tissue regions (Fig. 4d) 5 days post-injection, consistent with the observation made with *in vivo* optical imaging.

Verification of nanoprobes crossing the BBB without compromising the BBB

In our previous study, we have confirmed ND2:SmoA1 mouse model possesses an intact BBB (28). The accumulation of our nanoprobes in brain tumors as demonstrated by both MR and biophotonic imaging indicated that the nanoprobes overcame the BBB. However, the question remains whether the passage of the nanoparobes has compromised the BBB integrity. We verify the BBB integrity after the BBB crossing by the nanoprobe using the Evans blue exclusion assay. Two groups of ND2:SmoA1 mice were subjected to the assay: one group received NPCP-CTX and the other group received no nanoprobe treatment. Both groups were

administered with Evans blue dye, and their brains and lung/heart were imaged. No permeation of Evans blue into the brains of either group was observed (Supplementary Fig. 8), while, for comparison, the lungs/hearts of the same mice, which lack strict protective barriers like the BBB, exhibited significant blue staining due to dye permeation. These results (1) verified our previous studies utilizing immunostaining assessment that ND2:SmoA1 mice possess an intact BBB (28), and (2) confirmed that the passage of the nanoprobe left the BBB intact.

We further verified that the BBB in symptomatic ND2:SmoA1 mice were intact by the passage of the nanoprobe using Gd-DTPA exclusion method. In this method, permeation of intravenously injected Gd contrast agent into the brain tissue would indicate a compromised BBB (39). First, T1-weighted brain images were acquired for ND2:SmoA1 mice before and after receiving Gd-DTPA injection (Fig. 5a). Compared to the MR images of the mice before receiving Gd-DTPA (Fig. 5a, left), MR images of the cerebellum of these mice after Gd-DTPA administration showed that signal enhancement by Gd-DTPA was confined only to the neural vasculature and did not extend into the brain (Fig. 5a, right), confirming that ND2:SmoA1 mice possess an intact BBB. Next, the same mice were injected with NPCP-CTX; to confirm the entry of the nanoprobe into the brains, R2 maps of the cerebellums of these mice were acquired prior to and 48 hrs after NPCP-CTX administration (Fig. 5b). The significant R2 increase (red coloration) in the regions of the cerebellum where tumor tissue was expected after mice receiving NPCP-CTX (Fig. 5b, right), as compared to the same regions before nanoprobe injection (Fig.5b, left), indicates the entry of NPCP-CTX into the brains across the BBB and the accumulation in brain tumors. Then, the same mice were again injected with Gd-DPTA and T1-weighted imaging repeated before and after Gd-DPTA injection (Fig. 5c). Here again, the signal enhancement by Gd-DPTA was confined only to the neural vasculature, indicating that the BBB retained its integrity after the entry of the nanoprobe into the brain.

Nanoprobe biodistribution and toxicity profile

The biodistribution of the nanoprobes in mice receiving either NPCP-Cy5.5-CTX or NPCP-Cy5.5 was determined by *ex vivo* NIRF signal quantification of excised tissues (tumor, healthy brain tissue, heart, liver, spleen, kidney and muscle) 120 hrs post-injection of nanoprobes (Fig. 6). Here, tissues from mice receiving no nanoprobe injection were also presented to provide NIRF baseline signal intensities (intrinsic signals) for each of these tissues. No marked nanoprobe accumulation was observed in healthy brain tissue, heart, and muscle tissue ($P > 0.05$). NPCP-Cy5.5-CTX and NPCP-Cy5.5 accumulated at a similar level ($P > 0.05$) in each of these organs, indicating that the NPCP-Cy5.5-CTX has no specificity to these non-neoplastic tissues. Conversely, significant accumulation of the NPCP-Cy5.5-CTX nanoprobe ($P = 0.015$), but not the NPCP-Cy5.5, ($P > 0.05$) (note the baseline NIRF signals as exhibited by the mice receiving no injection), within tumor tissue further demonstrated high-level specificity and prolonged retention of NPCP-Cy5.5-CTX for tumor tissue. Additionally, the ability of the NPCP-Cy5.5-CTX nanoprobe to discriminate tumor from healthy tissue in brain, as demonstrated by MR and optical imaging, was further validated by its preferential accumulation within the brain tumor compared to normal brain tissue ($P = 0.0113$). It should be noted that significant nanoprobe accumulation in clearance organs including liver ($P < 0.0001$), spleen ($P < 0.001$), kidney ($P < 0.0001$) was expected, comparable in distribution profile to those reported for other iron oxide nanoparticle systems (40–42).

Since the accumulation of nanoprobes was expected to be the highest in liver, potential toxicity of the accumulated nanoprobes to liver was assessed by a hepatotoxicity assay. Serum aspartate aminotransferase (AST) and alanine aminotransferase (ALT) levels of mice injected with NPCP-Cy5.5-CTX or NPCP-Cy5.5 nanoprobes were measured (Supplementary Fig. 9). No marked elevation of AST ($P > 0.05$) and ALT ($P > 0.05$) levels was found in mice receiving

either nanoprobe compared to non-injected control mice, suggesting that neither nanoprobe induces liver toxicity at the given dosage.

In summary, we have developed a novel magnetofluorescent nanoprobe that is able to traverse the BBB, specifically target brain tumors, and leave BBB uncompromised. We revealed the significant difference between targeting and non-targeting nanoprobes in discrimination of tumor from healthy tissue. The nanoprobe has demonstrated persistent contrast enhancement for as long as 5 days. The MRI detectability combined with NIRF illumination exhibited by the same nanoprobe will potentially allow for more versatile uses of these contrast agents, such as preoperative diagnostics, tumor resection, as well as post-operative assessment with either MR or optical imaging. The developed nanoprobe platform retains the flexibility to conjugate alternative targeting and therapeutic agents, which may find its use for further development of alternative nanoparticle systems for specific applications.

Supplementary Material

Refer to Web version on PubMed Central for supplementary material.

Acknowledgments

References

1. Ferrari M. Cancer nanotechnology: Opportunities and challenges. Nature Reviews Cancer 2005;5:161–171.

2. Weissleder R. Molecular imaging in cancer. Science 2006;312:1168–1171. [PubMed: 16728630]

3. McNeil SE. Nanotechnology for the biologist. J Leukoc Biol 2005;78:585–594. [PubMed: 15923216]

4. Sun C, Lee JS, Zhang M. Magnetic nanoparticles in MR imaging and drug delivery. Adv Drug Deliv Rev 2008;60:1252–1265. [PubMed: 18558452]

5. Pardridge WM. The blood-brain barrier: bottleneck in brain drug development. NeuroRx 2005;2:3–14. [PubMed: 15717053]

6. Begley DJ. Delivery of therapeutic agents to the central nervous system: the problems and the possibilities. Pharmacol Ther 2004;104:29–45. [PubMed: 15500907]

7. Begley DJ. Understanding and circumventing the blood-brain barrier. Acta Paediatrica 2003;92:83–91.

8. Kaur IP, Bhandari R, Bhandari S, Kakkar V. Potential of solid lipid nanoparticles in brain targeting. J Control Release 2008;127:97–109. [PubMed: 18313785]

9. Kreuter J, Shamenkov D, Petrov V, et al. Apolipoprotein-mediated transport of nanoparticle-bound drugs across the blood-brain barrier. J Drug Target 2002;10:317–325. [PubMed: 12164380]

10. Kreuter J. Nanoparticulate systems for brain delivery of drugs. Adv Drug Deliv Rev 2001;47:65–81. [PubMed: 11251246]

11. Smith MW, Gumbleton M. Endocytosis at the blood-brain barrier: from basic understanding to drug delivery strategies. J Drug Target 2006;14:191–214. [PubMed: 16777679]

12. Ulbrich K, Hekmatara T, Herbert E, Kreuter J. Transferrin- and transferrin-receptor-antibody-modified nanoparticles enable drug delivery across the blood-brain barrier (BBB). Eur J Pharm Biopharm 2009;71:251–256. [PubMed: 18805484]

13. Rao KS, Reddy MK, Horning JL, Labhasetwar V. TAT-conjugated nanoparticles for the CNS delivery of anti-HIV drugs. Biomaterials 2008;29:4429–4438. [PubMed: 18760470]

14. Akhtari M, Bragin A, Cohen M, et al. Functionalized magnetonanoparticles for MRI diagnosis and localization in epilepsy. Epilepsia 2008;49:1419–1430. [PubMed: 18479391]

15. Brigger I, Morizet J, Aubert G, et al. Poly(ethylene glycol)-coated hexadecylcyanoacrylate nanospheres display a combined effect for brain tumor targeting. J Pharmacol Exp Ther 2002;303:928–936. [PubMed: 12438511]

16. Calvo P, Gouritin B, Villarroya H, et al. Quantification and localization of PEGylated polycyanoacrylate nanoparticles in brain and spinal cord during experimental allergic encephalomyelitis in the rat. European journal of neuroscience 2002;15:1317–1326. [PubMed: 11994126]

17. Silva GA. Nanotechnology approaches for drug and small molecule delivery across the blood brain barrier. Surg Neurol 2007;67:113–116. [PubMed: 17254859]

18. Silva GA. Neuroscience nanotechnology: progress, opportunities and challenges. Nat Rev Neurosci 2006;7:65–74. [PubMed: 16371951]

19. Sonavane G, Tomoda K, Makino K. Biodistribution of colloidal gold nanoparticles after intravenous administration: Effect of particle size. Colloids and Surfaces B-Biointerfaces 2008;66:274–280.

20. Sarin H, Kanevsky AS, Wu H, et al. Effective transvascular delivery of nanoparticles across the blood-brain tumor barrier into malignant glioma cells. J Transl Med 2008;6:80. [PubMed: 19094226]

21. Lu W, Wan J, Zhang Q, She Z, Jiang X. Aclarubicin-loaded cationic albumin-conjugated pegylated nanoparticle for glioma chemotherapy in rats. Int J Cancer 2007;120:420–431. [PubMed: 17066446]

22. Lu W, Wan J, She Z, Jiang X. Brain delivery property and accelerated blood clearance of cationic albumin conjugated pegylated nanoparticle. J Control Release 2007;118:38–53. [PubMed: 17240471]

23. Liu M, Li H, Luo G, Liu Q, Wang Y. Pharmacokinetics and biodistribution of surface modification polymeric nanoparticles. Arch Pharm Res 2008;31:547–554. [PubMed: 18449515]

24. Enochs WS, Harsh G, Hochberg F, Weissleder R. Improved delineation of human brain tumors on MR images using a long-circulating, superparamagnetic iron oxide agent. J Magn Reson Imaging 1999;9:228–232. [PubMed: 10077018]

25. Widder KJ, Morris RM, Poore G, Howard DP, Senyei AE. Tumor Remission in Yoshida Sarcoma-Bearing Rats by Selective Targeting of Magnetic Albumin Microspheres Containing Doxorubicin. Proceedings of the national academy of sciences of the united states of america-biological sciences 1981;78:579–581.

26. Lyons SA, O'Neal J, Sontheimer H. Chlorotoxin, a scorpion-derived peptide, specifically binds to gliomas and tumors of neuroectodermal origin. Glia 2002;39:162–173. [PubMed: 12112367]

27. Kachra Z, Beaulieu E, Delbecchi L, et al. Expression of matrix metalloproteinases and their inhibitors in human brain tumors. Clin Exp Metastasis 1999;17:555–566. [PubMed: 10845554]

28. Veiseh M, Gabikian P, Bahrami SB, et al. Tumor paint: a chlorotoxin:Cy5.5 bioconjugate for intraoperative visualization of cancer foci. Cancer Res 2007;67:6882–6888. [PubMed: 17638899]

29. Huwyler J, Wu D, Pardridge WM. Brain drug delivery of small molecules using immunoliposomes. Proc Natl Acad Sci U S A 1996;93:14164–14169. [PubMed: 8943078]

30. Shi N, Zhang Y, Zhu C, Boado RJ, Pardridge WM. Brain-specific expression of an exogenous gene after i.v. administration. Proc Natl Acad Sci U S A 2001;98:12754–12759. [PubMed: 11592987]

31. Pardridge WM. Drug and gene targeting to the brain with molecular Trojan horses. Nat Rev Drug Discov 2002;1:131–139. [PubMed: 12120094]

32. Fenart L, Casanova A, Dehouck B, et al. Evaluation of effect of charge and lipid coating on ability of 60-nm nanoparticles to cross an in vitro model of the blood-brain barrier. J Pharmacol Exp Ther 1999;291:1017–1022. [PubMed: 10565819]

33. Masciangioli T, Zhang WX. Environmental technologies at the nanoscale. Environ Sci Technol 2003;37:102A–108A.

34. Sontheimer H. An unexpected role for ion channels in brain tumor metastasis. Exp Biol Med (Maywood) 2008;233:779–791. [PubMed: 18445774]

35. Packer RJ, Cogen P, Vezina G, Rorke LB. Medulloblastoma: clinical and biologic aspects. Neuro-oncol 1999;1:232–250. [PubMed: 11550316]

36. Hallahan AR, Pritchard JI, Hansen S, et al. The SmoA1 mouse model reveals that notch signaling is critical for the growth and survival of sonic hedgehog-induced medulloblastomas. Cancer Res 2004;64:7794–7800. [PubMed: 15520185]

37. Bhattarai N, Matsen FA, Zhang M. PEG-Grafted Chitosan as an Injectable Thermoreversible Hydrogel. Macromol Biosci 2005;5:107–111. [PubMed: 15719428]

38. Veiseh O, Sun C, Gunn J, et al. An optical and MRI multifunctional nanoprobe for targeting gliomas. Nano Lett 2005;5:1003–1008. [PubMed: 15943433]

39. Hesselink JR, Press GA. MR contrast enhancement of intracranial lesions with Gd-DTPA. Radiol Clin North Am 1988;26:873–887. [PubMed: 3289078]

40. Moore A, Marecos E, Bogdanov A Jr, Weissleder R. Tumoral distribution of long-circulating dextran-coated iron oxide nanoparticles in a rodent model. Radiology 2000;214:568–574. [PubMed: 10671613]

41. Medarova Z, Pham W, Farrar C, Petkova V, Moore A. In vivo imaging of siRNA delivery and silencing in tumors. Nat Med 2007;13:372–377. [PubMed: 17322898]

42. Soroceanu L, Gillespie Y, Khazaeli MB, Sontheimer H. Use of chlorotoxin for targeting of primary brain tumors. Cancer Res 1998;58:4871–4879. [PubMed: 9809993]
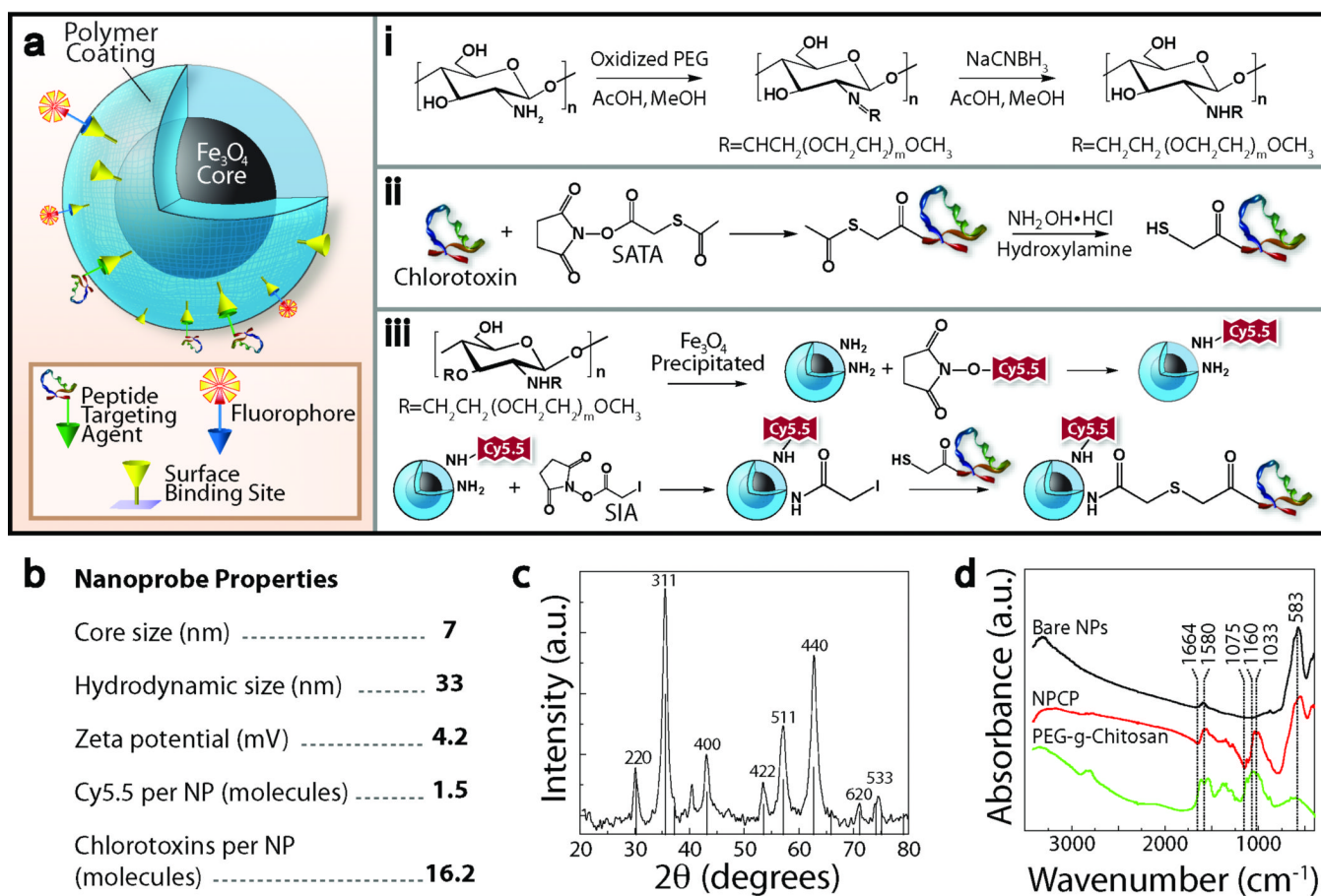
Figure 1.
Synthesis and characterization of NPCP-Cy5.5-CTX nanoprobes. Chemical reaction schematic for the syntheses of (**a**) PEG-grafted chitosan, (**b**) sulfhydryl functionalization of chlorotoxin (CTX), and (**c**) chlorotoxin and Cy5.5 conjugation to NPCP. (**d**) Summary of NPCP-Cy5.5-CTX physiochemical properties. (**e**) XRD diffraction pattern of NPCP confirming magnetite (Fe_3O_4) crystalline structure of the nanoprobe. (**f**) FTIR spectra of bare iron oxide nanoparticle, PEGylated chitosan, and NPCP, confirming successful immobilization of PEGylated chitosan on the surface of the nanoparticles.
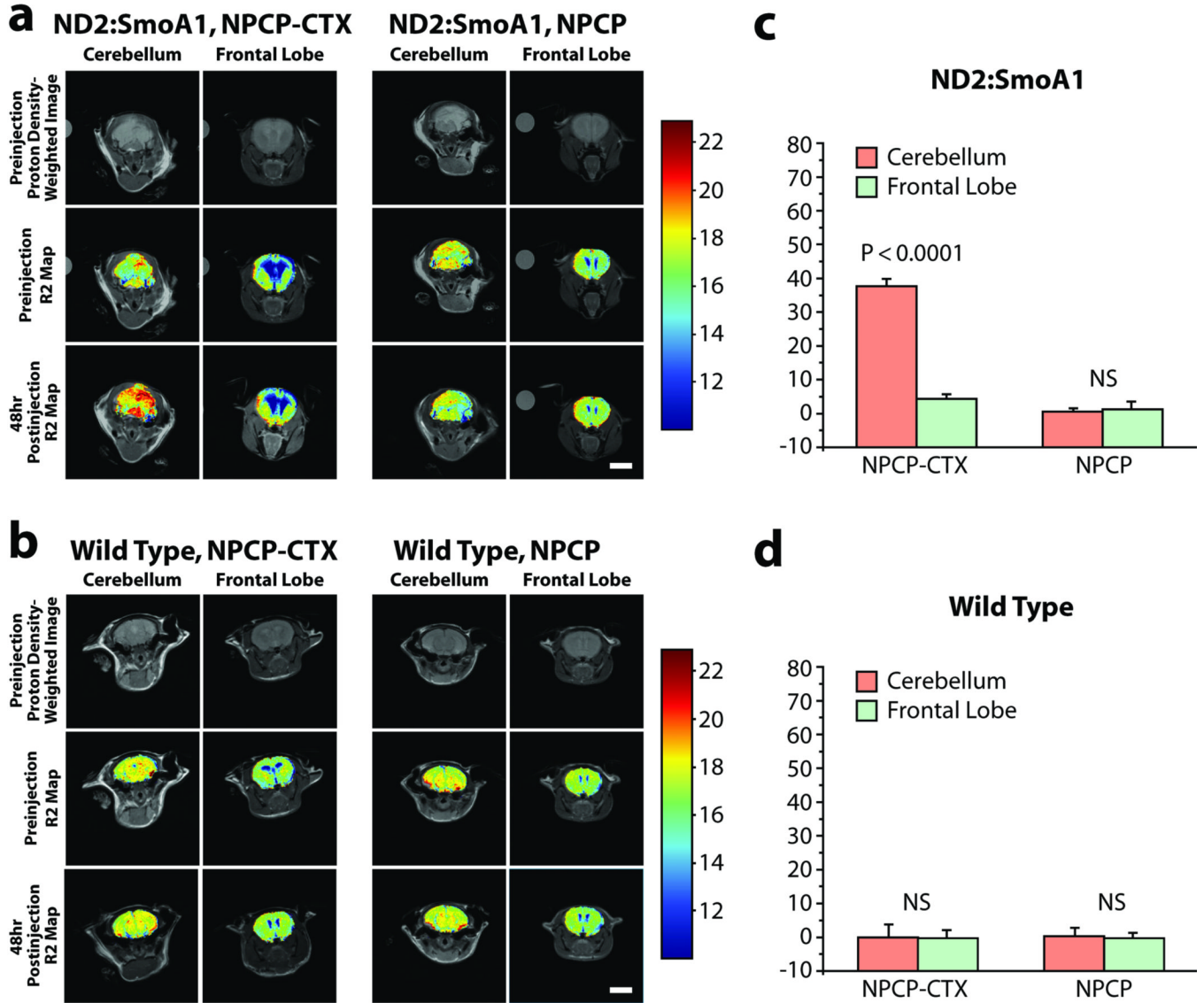
Figure 2.
In vivo MR imaging of brain tumors and signal quantification. *In vivo* MR images of (**a**) ND2:SmoA1 and (**b**) wild type mice acquired before and 48 hrs after administration of either NPCP-CTX or NPCP nanoprobes. Coronal cross sections of the frontal lobe (no tumor present) of the cerebral hemisphere and cerebellum (containing tumor tissues) were analyzed. Colorized R2 maps of the brain region were superimposed onto proton density-weighted images. Varying R2 values (s^{-1}) from low (blue) to high (red) were visually represented in colors generated from the gradient at right. Change in R2 was quantified by dividing the change in R2 before and after nanoprobe injection, by the pre-injection R2 response for (**c**) ND2:SmoA1 and (**d**) wild type mice. Both targeting (NPCP-CTX) and non-targeting (NPCP) nanoprobe systems were evaluated in ND2:SmoA1 and wild-type mice.
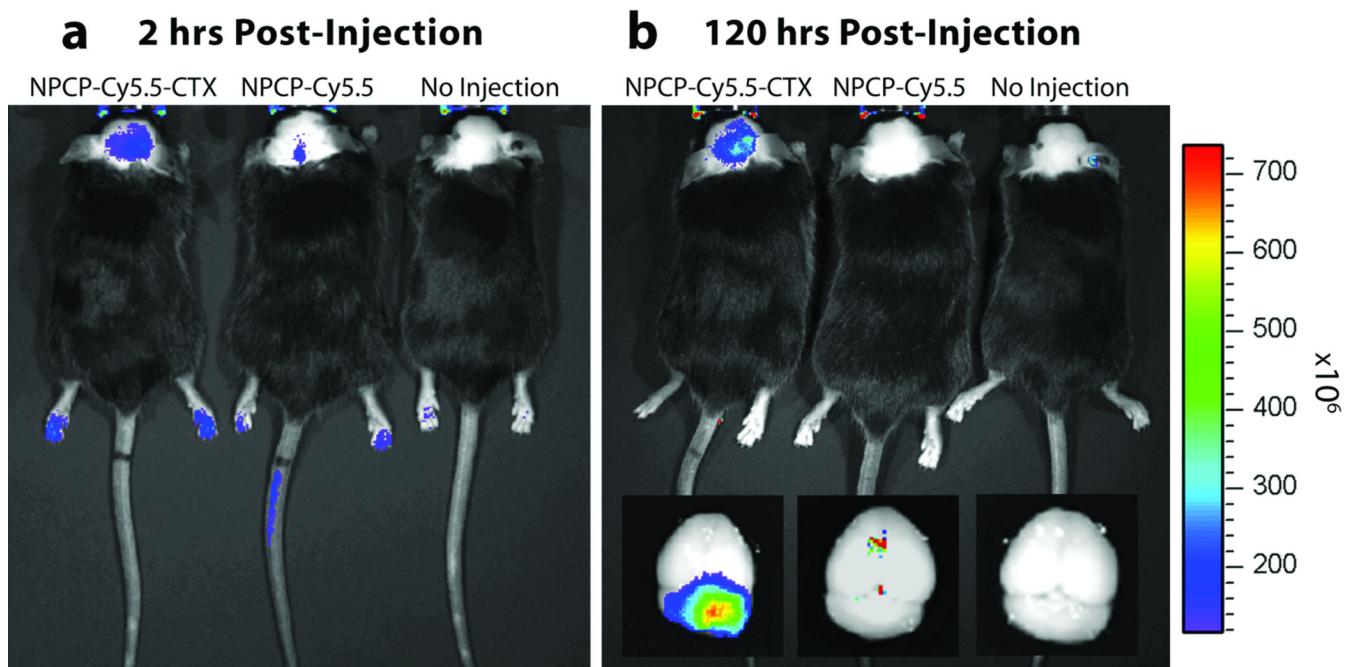
Figure 3.
In vivo NIRF imaging of autochthonous medulloblastoma tumors in genetically engineered ND2:SmoA1 mice. (**a** and **b**) Fluorescence imaging of medulloblastoma tumors in ND2:SmoA1 mice injected with either NPCP-Cy5.5-CTX or NPCP-Cy5.5, or receiving no injection (from left to right). Images were acquired at 2 hrs (**a**) and 120 hrs (**b**) post-injection. *Ex vivo* fluorescence images of mice brains from the same mice following necropsy are shown in the inset of **b**. The spectrum gradient bar at right corresponds to fluorescence intensity (p/s/cm^2/sr) of images.
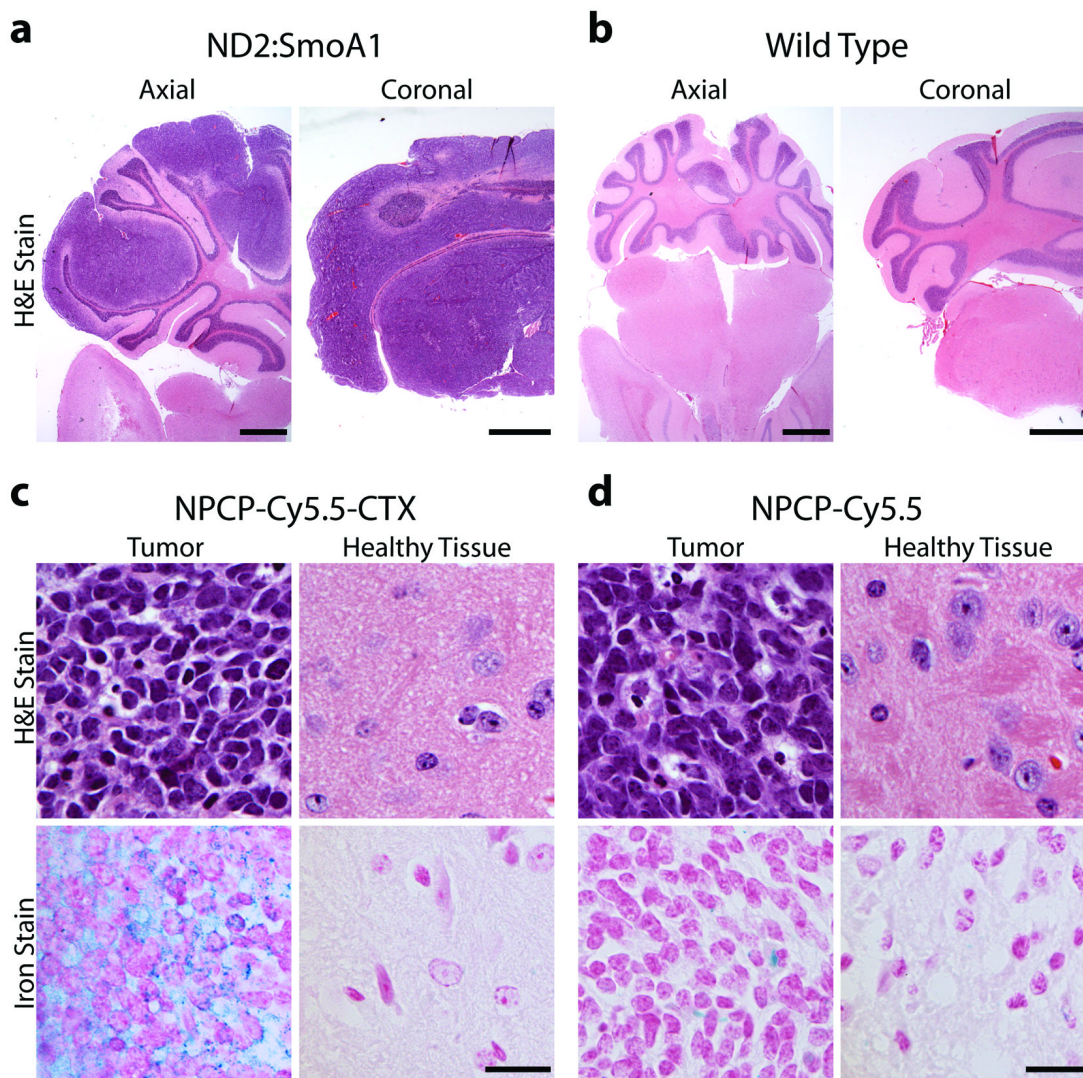
Figure 4.
Histological examination of mouse cerebellum 5 days post injection of NPCP-Cy5.5-CTX or NPCP-Cy5.5. (**a**) The H&E stained cerebellum section of symptomatic ND2:SmoA1 mice confirming presence of medulloblastoma, and (**b**) for comparison, the cerebellum of wild type mice showing normal cerebellum pathology (scale bars = 750 µm). (**c** and **d**) H&E and Prussian blue/nuclear fast red (iron stain) stained sections of cerebellum containing tumor and healthy brain tissues excised from mice receiving NPCP-Cy5.5-CTX (c) or NPCP-Cy5.5 (d), demonstrating preferential accumulation of NPCP-Cy5.5-CTX in medulloblastoma tumor tissues but not in healthy brain tissue, and minimal or no accumulation of NPCP-Cy5.5 in both tumor and healthy tissues (scale bars = 50 µm).
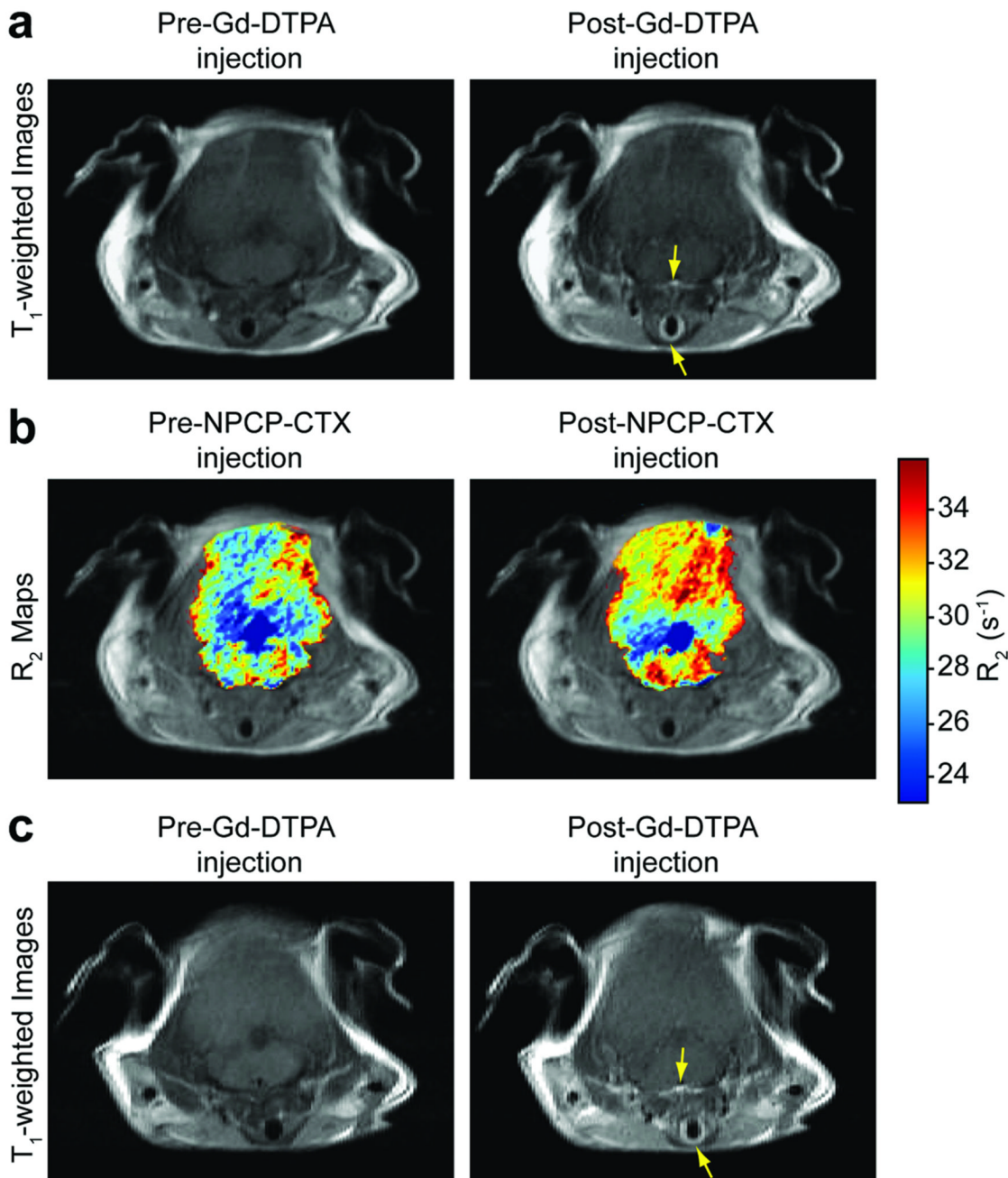
Figure 5.
Assessment of BBB integrity by Gd-DTPA exclusion prior to and post nanoprobe administration. (**a**) T1-weighted MR images (TR = 500 ms, TE = 14.7 ms) of N2:SmoA1 mice prior to and 5 minutes post-injection of Gd-DTPA. (**b**) Colorized R2 maps superimposed onto proton density-weighted images obtainted prior to and 48 hrs post injection of NPCP-CTX. Varying R2 values (s^{-1}) from low (blue) to high (red) were visually represented in a color bar scale at the right. (**c**) T1-weighted MR images (TR = 500 ms, TE = 14.7 ms) of N2:SmoA1 mice prior to and 5 minutes post injection of Gd-DTPA obtained 48 hrs after NPCP-CTX administration. Arrows indcate blood vessels.
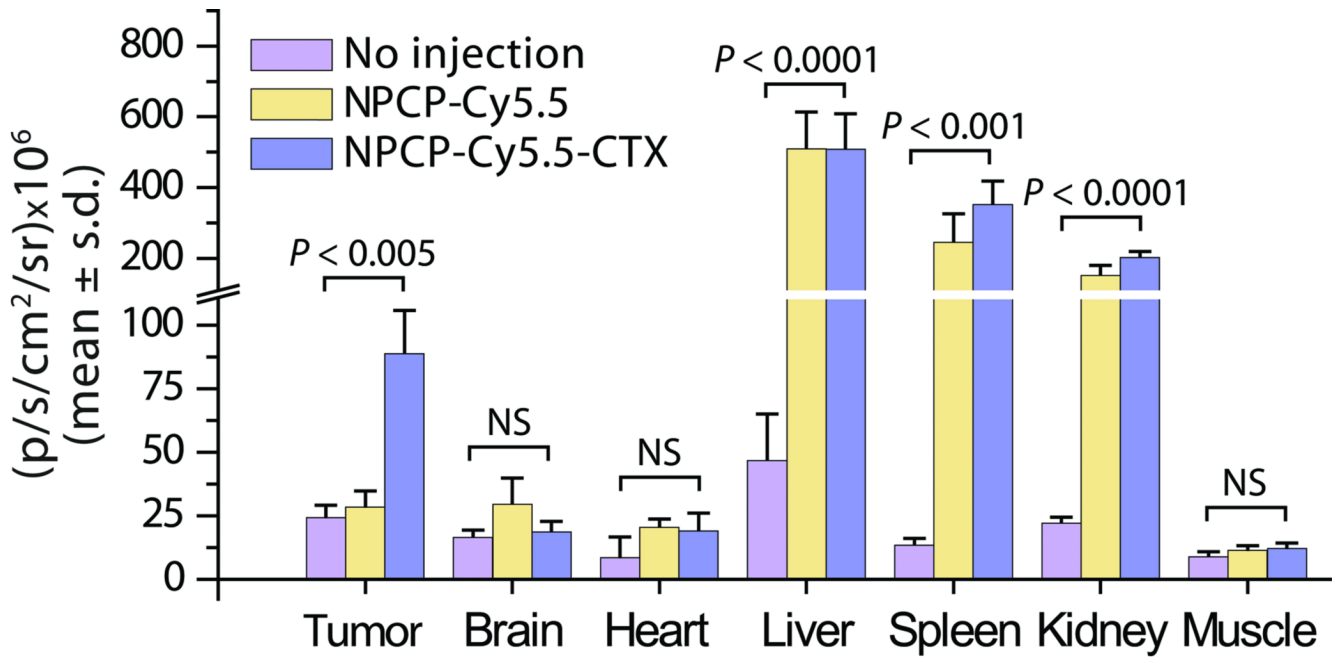
Figure 6.
Biodistribution of nanoprobes. Accumulation of nanoprobes in various tissues assessed by
NIRF signal measurements of tissues/organs excised from ND2:SmoA1 mice receiving no
injection and 120 hours after receiving injection of either targeting NPCP-Cy5.5-CTX or non-
targeting NPCP-Cy5.5.